



# A three-port isolated hybrid converter with wide range of voltage transformation ratio for DC microgrid

S. Sofiya<sup>1</sup> · Shelas Sathyan<sup>1</sup>

Received: 3 May 2023 / Accepted: 2 September 2023 / Published online: 27 September 2023  
© The Author(s), under exclusive licence to Springer-Verlag GmbH Germany, part of Springer Nature 2023

## Abstract

This paper presents a three-port isolated hybrid converter (3PIHC) with extended phase-shift modulation (EPM) to reduce voltage and current stress in the converter for DC microgrid applications. A high-frequency transformer with three independent windings is employed for isolating three ports in the converter. A wide variation in voltage transformation ratio is one of the main concern in DC microgrid, which need to be addressed for effective power conversion and utilization of the energy generation systems. Traditional phase-shift modulation (TPM) in 3PIHC leads to high conduction and core losses in the converter under wide variation in voltage transformation ratio. This paper proposes an extended phase-shift modulation in 3PIHC for different sequence of voltage transformation ratios between port 1 and port 2 ( $m_{12}$ ) and between port 1 and port 3 ( $m_{13}$ ), which is a cost-effective solution for reducing losses in the converter. The peak current at all ports and power equations in 3PIHC are deduced, and the computational method for obtaining the phase-shift values with minimum current stress is explained in detail. A comparative evaluation study proves that the proposed three-port converter with EPM outperforms to TPM in the aspects like low current stress, reduced semiconductor switching losses and transformer losses for wide variation in voltage transformation ratios. A hardware prototype of the proposed converter is built, and the results are evaluated and presented.

**Keywords** Extended phase-shift modulation · Three-port isolated hybrid converter · Traditional phase-shift modulation · Voltage transformation ratio

## 1 Introduction

Multiple energy generation units are essential for the reliable operation of power supply systems in microgrids. Factors such as integration of alternative power generation units, environmental effects, increasing energy demand and other economic aspects lead to a wide range of voltage variations in DC microgrids. In this scenario, productive power conversion and utilization can be achieved by employing an effective power electronic converter interface. A DC microgrid comprises multiple levels of DC bus voltages, namely high-voltage (HV), medium-voltage (MV) and low-voltage (LV) DC bus. In conventional system, two-port isolated DC–DC converter is employed for coupling the DC bus voltages. But, more number of DC–DC conversion units are required

and this will increase the size and cost of the system. The number of DC–DC conversion stages can be minimized by utilizing a three-port isolated converter. Figure 1 portrays the application of three-port isolated converter (3PIC) in DC microgrid. Here 3PIC is employed as a bidirectional link circuit among the three levels of DC bus voltage system. Here multiple voltage are generated from high-voltage (HV) DC bus using a single-stage 3PIC, where the number of conversion stages can be reduced compared to two-port two-stage converter [1, 2]. Port 1 is connected to HV DC bus system, and port 2 and port 3 are coupled to MV and LV DC bus system, respectively. Besides, 3PIC is an efficient choice in data centres for backup supply, where different load voltage divisions can be activated simultaneously.

Three-port isolated converter (3PIC) consists of three H-bridges and a three-winding high-frequency transformer. Leakage inductance of high-frequency transformer is a key element for energy transfer between the ports. Similar to two-port isolated converter the amount of power flow between the ports in a 3PIC is also determined by the phase-shift angles.

✉ S. Sofiya  
sfsanu@gmail.com

<sup>1</sup> National Institute of Technology, Tiruchirappalli, Tamil Nadu, India

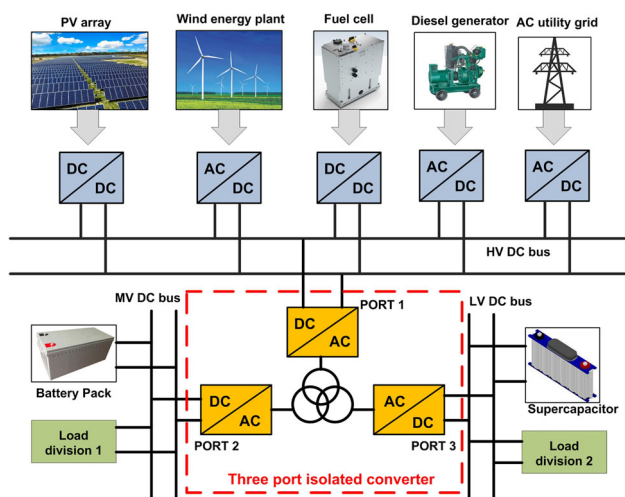


**Fig. 1** Three-port isolated converter in DC microgrid applications

The performance of 3PIC degrades when there is a voltage mismatch from the nominal value between the ports [3]. This may induce high current stress and associated losses in the converter. Two types of solutions are found in literature to minimize these challenges. One is by adding subcircuits to the power circuit, and another is by varying switch modulation strategies.

Power circuit transformation method includes LC series resonant 3PIC with phase-shift modulation [4], which involves tedious design procedures. A DC relay-based uni-directional three-port isolated series LC resonant converter is suggested in [5], for DC fast-charging applications. A power loss model of 3PIC is developed in [3] and [6]. In this, analysis is made to design the auxiliary inductance to minimize power losses in the converter. A dual transformer-based 3PIC is presented in [7], consisting of two high-frequency transformer; this avoids magnetic short circuit constraints and circulating power flow. Two inductor-based 3PICs is suggested in [8], which shows significant improvement in soft switching compared to conventional 3PIC. The paper [9] introduces a normalization design methodology of inductance in 3PIC based on port voltage variations and phase-shift values. Current fed multi-input-based DC–DC converter is put forward in [10], where the circuit operates in flux additive principle. Three-port half-bridge isolated converter is introduced in [11], where one of the port holds boost half-bridge configuration, to regulate the output voltage for a fuel cell-based system application. In all the above-mentioned cases, additional components will give rise to extra cost and size. An in-depth comparison of three-port converter topologies is attempted in [12], with regard to features, efficiency and practical aspects. The paper [13] evaluates three different winding configurations for high-frequency transformer in isolated converters, using finite element analysis method by considering different values of AC link current.

An alternative choice to advance the functionality of 3PIC is to utilize various switching modulation techniques. The basic modulation technique is the traditional phase-shift modulation (TPM), where phase-shifted switching signal is applied between bridges of port 1 and port 2, and between bridges of port 1 and port 3. If there is a variation in supply voltage or load voltage from the rated value, 3PIC is liable to high current stress and circulating current under TPM. A minimum circulating current is essential for attaining soft switching, as it flows through the leakage inductance of the transformer and charges the parasitic capacitance of the MOSFET. This stored energy then dissipated through the parasitic body diode of the MOSFET that is about to be conducted, thus providing zero voltage switching (ZVS) [14, 15]. The papers [16–18] recommend duty cycle control of 3PIC to minimize circulating current which involves broad calculations. 3PIC proposed in [19] employs same value of extra phase-shift in all bridges, which limits the variability scale of power flow and current transfer. Variable frequency modulation is initiated in [20] to improve the efficiency of the converter, but it requires complex numerical algorithms for finding the switch current and the required values of phase-shift. Various PWM techniques and configurations of isolated converters with its practical applications are discussed in [21] and [22], respectively. [23] discusses about the possible strategies to improve efficiency in isolated converters, which includes burst mode of switching operation, that is, by adjusting on-time and off-time of semiconductor switches, under very light load conditions. Extended phase-shift modulation (EPM) introduced in [24] offers numerous advantages over TPM. In this, besides the principal phase-shift an extra phase-shift is added between the limbs of either primary bridge (port 1) or secondary bridge (port 2), depending on the value of voltage transformation ratio. But the study and analysis are restricted to two-port isolated converter. The challenge related to applying EPM in 3PIC becomes significant when the voltage transformation ratios between the ports vary. This paper intends to analyse 3PIC with EPM and TPM schemes.

For high-voltage applications, H-bridges in isolated DC–DC converter is replaced by multilevel structures [25], so that the voltage stress across the semiconductor switches reduced to half of the supply voltage. This tends to operate the converter with low-voltage rated devices which minimize both switching and conduction losses. This paper focuses on developing an efficient three-port isolated converter to integrate different DC bus voltage levels in a DC microgrid and can operate at high efficiency during a wide change in voltage transformation ratios. A three-port isolated hybrid converter (3PIHC) with EPM scheme is proposed in this paper. The circuit consists of a multilevel half-bridge at the primary ( $1^0$ ) port and H-bridge configurations at the secondary ( $2^0$ ) and tertiary ( $3^0$ ) ports. The voltage across transformer primary will be

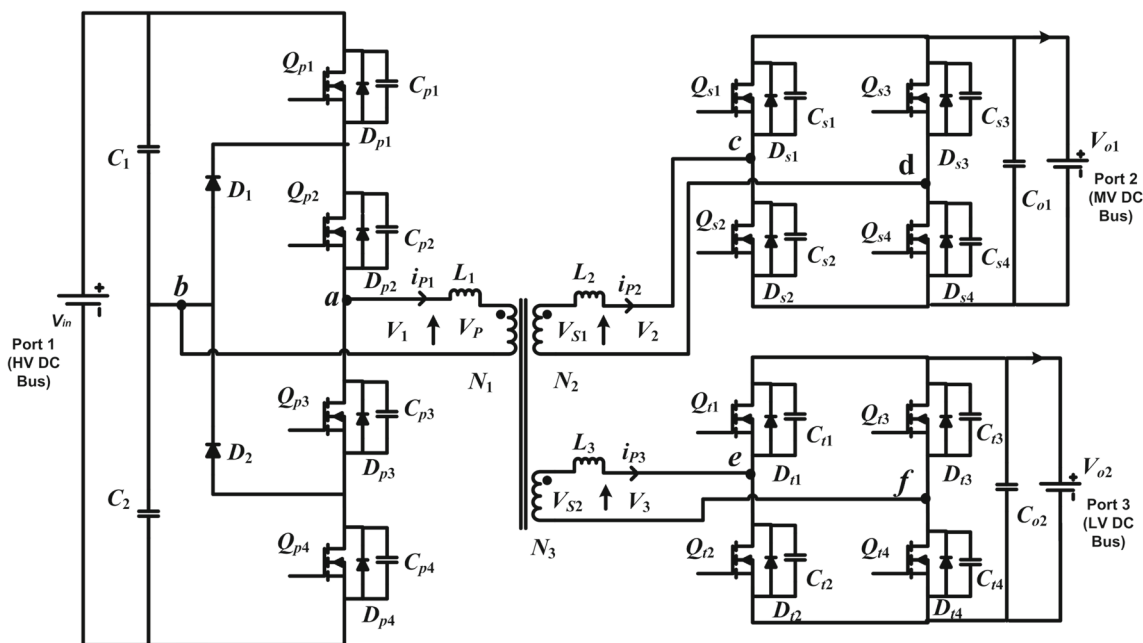


Fig. 2 Circuit diagram of three-port isolated hybrid converter

half of the supply voltage, which in turn reduces the turns ratio of the transformer.

The key contributions of this work are enumerated below,

1. Proposed a three-port isolated hybrid converter (3PIHC) which reduces the voltage stress across the primary winding of the transformer and semiconductor switching devices of primary port bridge.
2. Developed extended phase-shift modulation foremost to a three-port isolated converter.
3. Deduced power transfer equation and peak port current equations at all possible variations of voltage transformation ratio.
4. Simplified computational procedure is developed to attain the required phase-shift variables at minimum value of current stress. This reduces conduction loss in the converter.
5. Comparative loss analysis is performed between TPM and EPM schemes in the proposed 3PIHC.

Merits of the proposed converter with EPM scheme includes reduced voltage and current stress under wide variation in voltage transformation ratio, which consecutively deteriorate switching losses and conduction losses in the converter. Moreover, voltage waveforms with three levels across the transformer windings minimizes core losses.

The remaining part of the paper is organized, as follows: part 2 provides steady-state time-domain analysis of 3PIHC with EPM strategy, power transfer analysis between the ports under EPM and TPM schemes, comparative anal-

ysis of current stress between EPM and TPM techniques and optimization. Part 3 gives the description about hardware implementation and experimental waveforms, and part 4 outlines conclusions.

## 2 Steady-state time-domain analysis of proposed 3PIHC with EPM strategy

The proposed topology of 3PIHC is shown in Fig. 2. Here, the 1<sup>0</sup> side port is coupled to high-voltage DC bus, and 2<sup>0</sup> side port and 3<sup>0</sup> side port are linked to medium- and low-voltage DC bus systems, respectively. In the conventional 3PIC [16], all the ports hold H-type bridge configurations. In the proposed topology, 1<sup>0</sup> side of the port is replaced by multilevel half-bridge structure, which will lessen the voltage across switches and transformer 1<sup>0</sup> winding to half of the supply voltage. This in turn decreases the number of turns in the transformer compared with conventional 3PIC.

The three-winding high-frequency transformer are designed on the basis of voltage levels at the three respective ports. In the circuit,  $N_1 : N_2 : N_3$  represents winding ratio of three-winding transformer.  $L_1, L_2$  and  $L_3$  denote leakage inductance of three-winding transformer at the three successive ports. The equivalent transformer voltage at 1<sup>0</sup>, 2<sup>0</sup> and 3<sup>0</sup> windings is given by  $V_P, V_{S1}$  and  $V_{S2}$ , respectively. The voltage magnitudes referred to 1<sup>0</sup> side of the transformer are given by  $V_1, V_2$  and  $V_3$ , where  $V_1 = V_{in}/2$ .  $i_{P1}, i_{P2}$  and  $i_{P3}$  are the respective port currents at 1<sup>0</sup>, 2<sup>0</sup> and 3<sup>0</sup> winding, respectively.

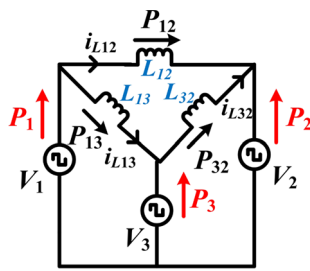


Fig. 3 Equivalent circuit model of three-winding transformer in 3PIHC

In TPM, a phase-shifted gate signal is applied to port 2 with reference to port 1, which results in two square waveforms with a phase difference of  $\alpha_2$ , across the leakage inductance of the transformer windings; this leads to power flow from port 1 towards port 2. Similarly, a phase-shifted gate pulse of phase difference  $\alpha_3$  is applied to port 3 with reference to port 1, which directs the power transfer from port 1 towards port 3. To reverse the power transfer, apply a phase-shifted gate signal to port 1 with reference to port 3 [26]. In general, the phase-shifted signal variables applied depends on power demand and voltage transformation ratios between the ports.

The equivalent circuit model of three-winding transformer referred to  $1^0$  side in 3PIHC is illustrated in Fig. 3; here, the currents flowing through the leakage inductances  $L_{12}$ ,  $L_{13}$  and  $L_{32}$  are denoted as  $i_{L12}$ ,  $i_{L13}$  and  $i_{L32}$ , respectively. The voltage transformation ratios among the ports are interpreted as  $m_{12} = \frac{V_2}{V_1}$  and  $m_{13} = \frac{V_3}{V_1}$ . If the value of voltage transformation ratio differs from unity, transformer windings and semiconductor switches in the converter are subjected to increased current stress [3]. To minimize this current stress and associated power losses at wide variation in voltage transformation ratio, this paper proposes EPM for 3PIHC. In general, for EPM, an additional phase-shift is applied based on the value of port voltages. In case of two-port converter, if the voltage transformation ratio  $m$  (let  $m = \frac{V_2}{V_1}$ ) is less than one, then an extra phase-shift is applied to the primary side bridge, and if  $m$  is greater than one, an additional phase-shift is applied to the secondary side bridge [24].

In the proposed topology, four possible combinations of voltage transformation ratio of  $m_{12}$  and  $m_{13}$  exist and are as follows (i) EPM-Case A:  $(m_{12} \wedge m_{13}) \leq 1$ ; (ii) EPM-Case B:  $(m_{12} \wedge m_{13}) > 1$ ; (iii) EPM-Case C:  $(m_{12} > 1) \wedge (m_{13} \leq 1)$ ; and (iv) EPM-Case D:  $(m_{12} \leq 1) \wedge (m_{13} > 1)$ . The power transfer flexibility and deduction in current stress are the major aspects which improves the performance of the 3PIHC in EPM scheme. The power flow expressions among the ports and peak value of current equations at all the ports are deduced with respect to  $m_{12}$  and  $m_{13}$  to evaluate the performance of 3PIHC in both EPM and TPM techniques.

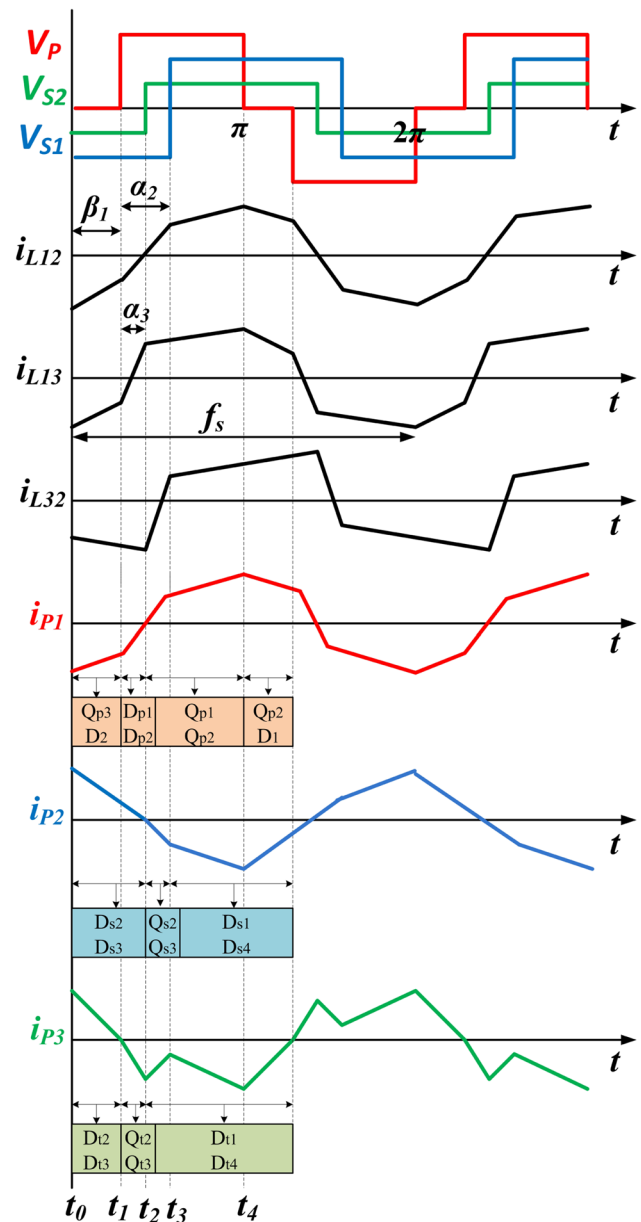


Fig. 4 Steady-state time-domain waveforms in 3PIHC for EPM-Case A:  $(m_{12} \wedge m_{13}) \leq 1$

Consider that the 3PIHC is operating under steady-state condition, and for time-domain analysis, the case examined is EPM-Case A:  $(m_{12} \wedge m_{13}) \leq 1$ . Here the power flow accounted is from port 1 towards port 2 and port 3. The elements in conduction and the switching time intervals are illustrated in Fig. 4. The intervals of operation of 3PIHC are divided into four modes and are explained accordingly:

1. Mode I ( $t_0 - t_1$ )—Prior to time  $t_0$ , the switch elements in conduction at port 1 bridge are  $Q_{p3}$  and  $Q_{p4}$ . At time  $t_0$ ,  $Q_{p4}$  is switched OFF and  $Q_{p3}$  continues to be active, due to the extra phase-shift  $\beta_1$  applied between

**Table 1** Instantaneous time-domain current expressions of 3PIHC with EPM scheme

	$i_{L12}$	$i_{L13}$	$i_{L32}$
Mode I	$\frac{V_1 m_{12}}{\omega L_{12}} (t - t_0) + i_{L12}(t_0)$	$\frac{V_1 m_{13}}{\omega L_{13}} (t - t_0) + i_{L13}(t_0)$	$\frac{V_1 (m_{12} - m_{13})}{\omega L_{32}} (t - t_0) + i_{L32}(t_0)$
Mode II	$\frac{V_1 (1 + m_{12})}{\omega L_{12}} (t - t_1) + i_{L12}(t_1)$	$\frac{V_1 (1 + m_{13})}{\omega L_{13}} (t - t_1) + i_{L13}(t_1)$	$\frac{V_1 (m_{12} - m_{13})}{\omega L_{32}} (t - t_1) + i_{L32}(t_1)$
Mode III	$\frac{V_1 (1 + m_{12})}{\omega L_{12}} (t - t_2) + i_{L12}(t_2)$	$\frac{V_1 (1 - m_{13})}{\omega L_{13}} (t - t_2) + i_{L13}(t_2)$	$\frac{V_1 (m_{12} + m_{13})}{\omega L_{32}} (t - t_2) + i_{L32}(t_2)$
Mode IV	$\frac{V_1 (1 - m_{12})}{\omega L_{12}} (t - t_3) + i_{L12}(t_3)$	$\frac{V_1 (1 - m_{13})}{\omega L_{13}} (t - t_3) + i_{L13}(t_3)$	$\frac{V_1 (m_{13} - m_{12})}{\omega L_{32}} (t - t_3) + i_{L32}(t_3)$

$Q_{p3}$  and  $Q_{p4}$ . The conduction path by referring to Fig. 2 is given by  $a \rightarrow Q_{p3} \rightarrow D_2 \rightarrow b \rightarrow L_1 \rightarrow a$ , which results into zero voltage state across the 1<sup>0</sup> winding of the transformer. In the 2<sup>0</sup> side port of Fig. 2,  $D_{s2}$  and  $D_{s3}$  are active, and the conduction path is given by  $d \rightarrow D_{s3} \rightarrow C_{o1} \rightarrow D_{s2} \rightarrow c \rightarrow L_2 \rightarrow d$ . Similarly, in the 3<sup>0</sup> side port,  $D_{t2}$  and  $D_{t3}$  conducts, the current direction path is specified as  $f \rightarrow D_{t3} \rightarrow C_{o2} \rightarrow D_{t2} \rightarrow e \rightarrow L_3 \rightarrow f$ . The current equations between the ports with reference to voltage transformation ratio and time instants are given in Table 1.

- Mode II ( $t_1 - t_2$ )—In this mode, as the gate pulses are given to  $Q_{p1}$  and  $Q_{p2}$  at time  $t_1$ , it remains in OFF state due to the energy stored in parasitic capacitors  $C_{p1}$  and  $C_{p2}$ . This stored energy is discharged through antiparallel diodes  $D_{p1}$  and  $D_{p2}$ , thus directing towards zero voltage switch ON state for  $Q_{p1}$  and  $Q_{p2}$ . The conduction path by referring to Fig. 2 is indicated as  $a \rightarrow D_{p2} \rightarrow D_{p1} \rightarrow C_1 \rightarrow b \rightarrow L_1 \rightarrow a$ . The elements in conduction and the current track at the 2<sup>0</sup> bridge port is same as in mode I. On the tertiary side bridge,  $Q_{t2}$  and  $Q_{t3}$  are turned ON at zero voltage switching. The current trace in bridge at port 3 is given by  $e \rightarrow Q_{t2} \rightarrow C_{o2} \rightarrow Q_{t3} \rightarrow f \rightarrow L_3 \rightarrow e$ . The current expressions between the ports is given by equations in Table 1.
- Mode III ( $t_2 - t_3$ )—In this mode, switches in the primary side bridge  $Q_{p1}$  and  $Q_{p2}$  are turned on at zero voltage state. The current transfer path by referring to Fig. 2 is given by  $C_1 (V_{in}/2) \rightarrow Q_{p1} \rightarrow Q_{p2} \rightarrow a \rightarrow L_1 \rightarrow b \rightarrow C_1$ . In the 2<sup>0</sup> side bridge,  $Q_{s2}$  and  $Q_{s3}$  are turned on at zero voltage switching. The conduction path is represented as,  $c \rightarrow Q_{s2} \rightarrow C_{o1} \rightarrow Q_{s3} \rightarrow d \rightarrow L_2 \rightarrow c$ . On the 3<sup>0</sup> side bridge, the energy stored in  $C_{t1}$  and  $C_{t4}$  are discharged through  $D_{t1}$  and  $D_{t4}$ . The current direction is given by  $e \rightarrow D_{t1} \rightarrow C_{o2} \rightarrow D_{t4} \rightarrow f \rightarrow L_3 \rightarrow e$ . The current equations between the ports are represented in Table 1.
- Mode IV ( $t_3 - t_4$ )—In the primary side,  $Q_{p1}$  and  $Q_{p2}$  continues conduction same as before. The direction of conduction path is equivalent to mode III. On the 2<sup>0</sup> side bridge, at time  $t_3$ , gate signals are fed to  $Q_{s1}$  and  $Q_{s4}$ , but it will not start to conduct, as the stored energy in  $C_{s1}$  and

$C_{s4}$  are discharging through  $D_{s1}$  and  $D_{s4}$ . The direction of current transfer by referring to Fig. 2 is indicated as  $c \rightarrow D_{s1} \rightarrow C_{o1} \rightarrow D_{s4} \rightarrow d \rightarrow L_2 \rightarrow c$ . In the 3<sup>0</sup> bridge,  $D_{t1}$  and  $D_{t4}$  continues conduction similar to mode III. The current path holds same as in previous mode. The current expressions between the ports are indicated in Table 1.

### 2.1 Analysis of power transfer between the ports under EPM and TPM schemes

The phase-shift angles applied in 3PIHC is the main decision variables which determines the amount of power transfer among the ports. The general expression for obtaining the power transferred among the ports is given in equation (1) [24]. It is the average of function attained by multiplying current fed among the ports with supply voltage over half switching interval  $[0, \pi]$ .

$$P = \frac{V}{\pi} \int_0^\pi i_L(t) \tag{1}$$

Replace the time intervals in current equations given in Table 1 as follows:  $t_0=0, t_1=\beta_1, t_2=\beta_1+\alpha_3, t_3=\beta_1+\alpha_2$  and  $t_4=\pi$ , and substituting it in Eq. (1) leads to power transfer expressions among the ports in EPM-Case A and is expressed as follows [24, 26],

$$P_{12} = \frac{V_1^2 m_{12}}{\omega \pi L_{12}} [\alpha_2 (\pi - \alpha_2) + 0.5 \beta_1 (\pi - \beta_1 - 2\alpha_2)] \tag{2}$$

$$P_{13} = \frac{V_1^2 m_{13}}{\omega \pi L_{13}} [\alpha_3 (\pi - \alpha_3) + 0.5 \beta_1 (\pi - \beta_1 - 2\alpha_3)] \tag{3}$$

$$P_{32} = \frac{V_1^2 m_{12} m_{13}}{\omega \pi L_{32}} [|\alpha_2 - \alpha_3| (\pi - |\alpha_2 - \alpha_3|)] \tag{4}$$

where the range of variables is given by,

$$0 \leq \beta_1 \leq \pi, 0 \leq \alpha_2 \leq \pi, 0 \leq (\beta_1 + \alpha_2) \leq \pi$$

$$0 \leq \alpha_3 \leq \pi, 0 \leq (\beta_1 + \alpha_3) \leq \pi$$

The resulting power flow at each port is deduced as  $P_1 = P_{12} + P_{13}, P_2 = -P_{12} - P_{32}$  and  $P_3 = -P_{13} + P_{32}$  [16].

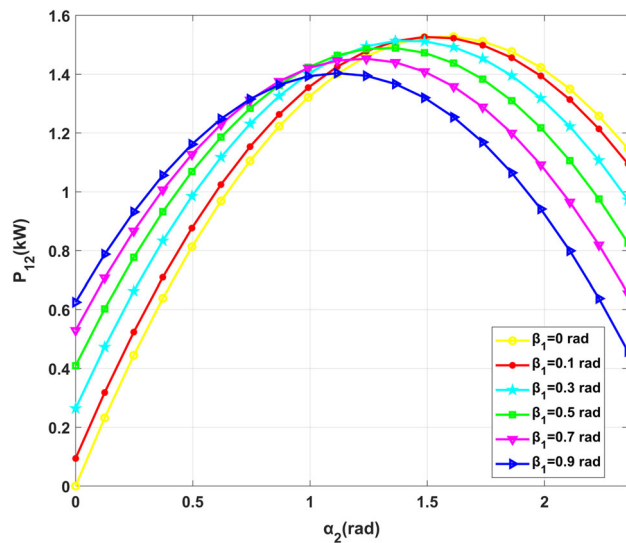


**Fig. 5** Power transfer characteristics ( $P_{12}$ ) with respect to phase-shift angle  $\alpha_2$

In 3PIHC for TPM, only the principle phase-shift variables  $\alpha_2$  and  $\alpha_3$  exist; therefore, the power flow expression for TPM is achieved by replacing  $\beta_1$  as zero in Eqs. (2) and (3). Figure 5 presents power flow characteristics among the ports 1 and 2 with reference to phase-shift angle  $\alpha_2$  at specified quantities of  $\beta_1$ . The curve corresponds to  $\beta_1$  equal to zero indicates the power flow in TPM scheme. From the characteristics, it is clear that maximum amount of power is transferred at a phase-shift angle equal to 1.57 rad ( $\pi/2$ ) in both EPM and TPM scheme. By changing the value of  $\beta_1$ , the adaptability of power transfer characteristics is enhanced and it upgrades the variability to select phase-shift angles  $\alpha_2$  according to the power demand and converter performance. For EPM-Case B: when  $(m_{12} \wedge m_{13}) > 1$ , in addition to main phase-shift  $\alpha_2$  and  $\alpha_3$ , extra phase-shift  $\beta_2$  and  $\beta_3$  are applied to port 2 and port 3 bridge, respectively. The steady-state waveforms and the devices in conduction in each ports are illustrated in Fig. 6a. In this case, the power equation  $P_{12}$  and  $P_{13}$  are obtained as below [24, 26],

$$P_{12} = \frac{V_1^2 m_{12}}{\omega \pi L_{12}} [\alpha_2 (\pi - \alpha_2) + 0.5 \beta_2 (\pi - \beta_2 - 2\alpha_2)] \quad (5)$$

$$P_{13} = \frac{V_1^2 m_{13}}{\omega \pi L_{13}} [\alpha_3 (\pi - \alpha_3) + 0.5 \beta_3 (\pi - \beta_3 - 2\alpha_3)] \quad (6)$$

where the range of variables is defined as,

$$0 \leq \beta_2 \leq \pi, 0 \leq \alpha_2 \leq \pi, 0 \leq (\beta_2 + \alpha_2) \leq \pi, 0 \leq \beta_3 \leq \pi, \\ 0 \leq \alpha_3 \leq \pi, 0 \leq (\beta_3 + \alpha_3) \leq \pi$$

For EPM-Case C: when  $(m_{12} > 1) \wedge (m_{13} \leq 1)$ , in addition to main phase-shift  $\alpha_2$  and  $\alpha_3$ , extra phase-shift  $\beta_2$  is applied to port 2 bridge as  $(m_{12} > 1)$  and  $\beta_1$  is applied to port

1 bridge as  $(m_{13} \leq 1)$ . The steady-state waveforms along with the elements in conduction is depicted in Fig. 6b. The power equation  $P_{12}$  given in Table 2 is obtained for three sets of intervals, as port 1–port 2 comprise of two different extra phase-shift variables  $\beta_1$  and  $\beta_2$ . Intervals are classified based on the level of power transfer,  $P_{12}$  corresponds to low-, medium- and high-power ranges are  $(0 \leq \alpha_2 \leq (\alpha_2 + \beta_2) \leq \beta_1 \leq \pi)$ ,  $(0 \leq \alpha_2 \leq \beta_1 \leq (\alpha_2 + \beta_2) \leq \pi)$ , and  $(0 \leq \beta_1 \leq \alpha_2 \leq (\alpha_2 + \beta_2) \leq \pi)$ , respectively. Power equation  $P_{13}$  remains same as per equation (3), as port 1–port 3 comprise of only one extra phase-shift  $\beta_1$ .

For EPM-Case D: when  $(m_{12} \leq 1) \wedge (m_{13} > 1)$ , in spite of principal phase-shift  $\alpha_2$  and  $\alpha_3$ , additional phase-shift  $\beta_1$  is applied to port 1 bridge as  $(m_{12} \leq 1)$  and  $\beta_3$  is applied to port 3 bridge as  $(m_{13} > 1)$ . The steady-state operational waveform, along with the device in conduction is presented in Fig. 6c. Similar to EPM-Case C, the power transfer equation for  $P_{13}$  in Table 2 is determined for three sets of intervals, based on the level of power transfer, as port 1–port 3 encompass two different extra phase-shift variables  $\beta_1$  and  $\beta_3$ .  $P_{12}$  holds same as per Eq. (2), where only one extra phase-shift  $\beta_1$  is applied between port 1 and port 2.

### 2.2 Comparative analysis of current stress between EPM and TPM techniques and optimization

The peak port current expressions in 3PIHC is deduced in terms of phase-shift variables and voltage transformation ratio  $m_{12}$  and  $m_{13}$  to evaluate the performance of converter in EPM and TPM techniques. The time-domain current equations for EPM-Case A  $(m_{12} \wedge m_{13}) \leq 1$  is derived and presented in Table 1. The time instants defined with respect to phase-shift variables are as follows,  $t_1 = \beta_1$ ,  $t_2 = \beta_1 + \alpha_3$ ,  $t_3 = \beta_1 + \alpha_2$  and  $t_4 = \pi$ . To reduce the complexity in current expressions, the leakage inductance of the transformer with referred to  $1^0$  side is assumed to be similar, that is,  $L_{12} = L_{13} = L_{32} = L$ . The general expression for port current is indicated below [16],

$$i_{P1}(t) = i_{L12}(t) + i_{L13}(t) \\ i_{P2}(t) = -i_{L12}(t) - i_{L32}(t) \\ i_{P3}(t) = -i_{L13}(t) + i_{L32}(t) \quad (7)$$

Defining the expressions of  $i_{L12}(t)$ ,  $i_{L13}(t)$  and  $i_{L32}(t)$  in terms of phase-shift variables and substituting it in Eq. (7) direct towards port current equations as mentioned in Table 3.

Similarly the current stress in each port for EPM-Case B:  $(m_{12} \wedge m_{13}) > 1$ , EPM-Case C:  $(m_{12} > 1) \wedge (m_{13} \leq 1)$  and EPM-Case D:  $(m_{12} \leq 1) \wedge (m_{13} > 1)$  are computed and listed in Tables 3, 4 and 5, respectively.

According to the voltage transformation ratio and power requirement, appropriate value of phase-shift angles needs

**Table 2** Power transfer between the ports for EPM-Case C and EPM-Case D

Time interval	$P_{12}$ for EPM-Case C
$(0 \leq \alpha_2 \leq (\alpha_2 + \beta_2) \leq \beta_1 \leq \pi)$	$\frac{V_1^2 m_{12}}{\omega \pi L_{12}} [(\pi - \beta_1) (2\alpha_2 + \beta_2 - \beta_1)]$
$(0 \leq \alpha_2 \leq \beta_1 \leq (\alpha_2 + \beta_2) \leq \pi)$	$\frac{V_1^2 m_{12}}{\omega \pi L_{12}} [2\alpha_2 (\pi - \beta_2) + \beta_2 (\pi - \beta_2 + \beta_1) - \beta_1 - \alpha_2^2]$
$(0 \leq \beta_1 \leq \alpha_2 \leq (\alpha_2 + \beta_2) \leq \pi)$	$\frac{V_1^2 m_{12}}{\omega \pi L_{12}} [\beta_1 (2\alpha_2 + \beta_2 - \beta_1 - \pi) + \beta_2 (\pi - \beta_2 - 2\alpha_2) - 2\alpha_2^2 + 2\alpha_2]$
Time interval	$P_{13}$ for EPM-Case D
$(0 \leq \alpha_3 \leq (\alpha_3 + \beta_3) \leq \beta_1 \leq \pi)$	$\frac{V_1^2 m_{13}}{\omega \pi L_{13}} [(\pi - \beta_1) (2\alpha_3 + \beta_3 - \beta_1)]$
$(0 \leq \alpha_3 \leq \beta_1 \leq (\alpha_3 + \beta_3) \leq \pi)$	$\frac{V_1^2 m_{13}}{\omega \pi L_{13}} [2\alpha_3 (\pi - \beta_3) + \beta_3 (\pi - \beta_3 + \beta_1) - \beta_1 - \alpha_3^2]$
$(0 \leq \beta_1 \leq \alpha_3 \leq (\alpha_3 + \beta_3) \leq \pi)$	$\frac{V_1^2 m_{13}}{\omega \pi L_{13}} [\beta_1 (2\alpha_3 + \beta_3 - \beta_1 - \pi) + \beta_3 (\pi - \beta_3 - 2\alpha_3) - 2\alpha_3^2 + 2\alpha_3]$

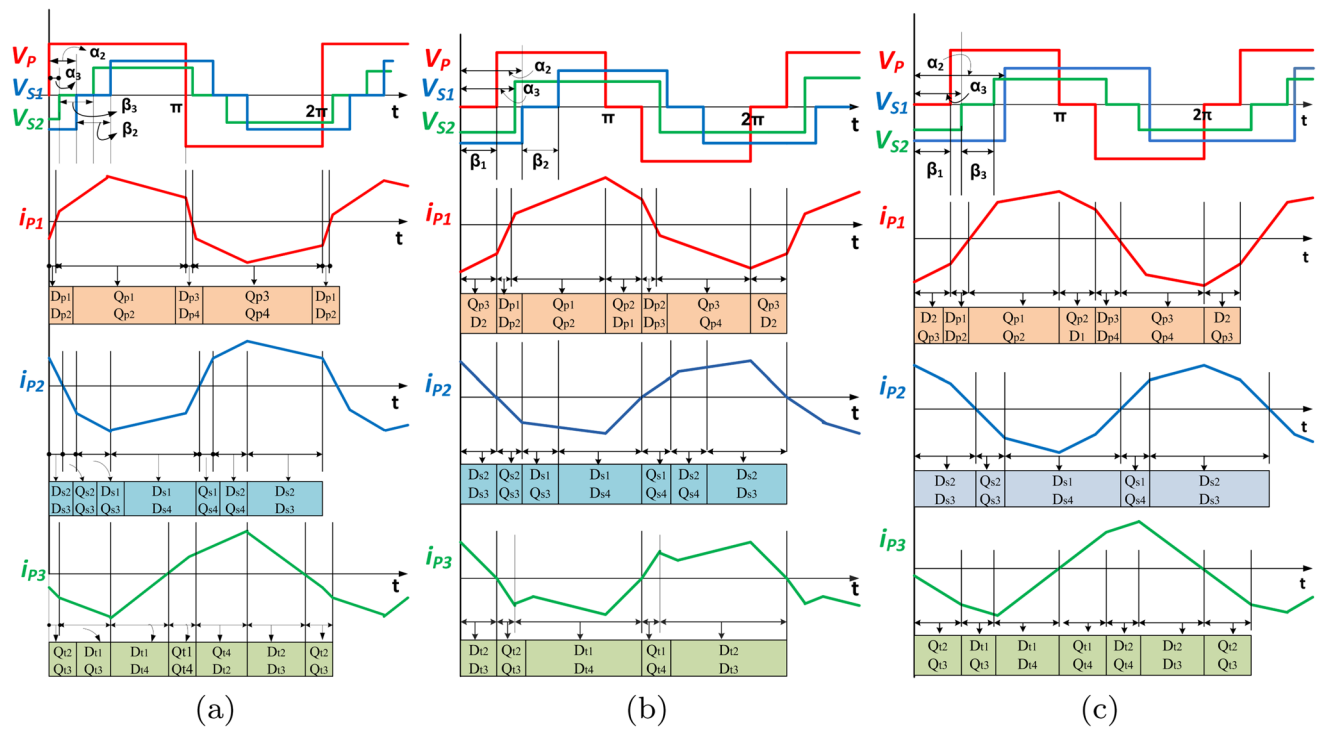


**Fig. 6** Steady-state time-domain waveforms for (a) EPM-Case B:  $(m_{12} \wedge m_{13}) > 1$ . (b) EPM-Case C:  $(m_{12} > 1) \wedge (m_{13} \leq 1)$ . (c) EPM-Case D:  $(m_{12} \leq 1) \wedge (m_{13} > 1)$

**Table 3** Port current expressions for EPM-Case A and EPM-Case B

Port current equations for EPM-Case A	
$i_{P1 \max}$	$\frac{V_1}{2\omega L} \{ 2(\pi - \beta_1) - m_{12}(\pi - 2\alpha_2 - 2\beta_1) - m_{13}(\pi - 2\alpha_3 - 2\beta_1) \}$
$i_{P2 \max}$	$\frac{V_1}{2\omega L} \{ (\pi - \beta_1) - 2m_{12}(\pi - 2\alpha_2 - 2\beta_1) + m_{13}(\pi - 2\alpha_3 - 2\beta_1) \}$
$i_{P3 \max}$	$\frac{V_1}{2\omega L} \{ (\pi - \beta_1) - 2m_{13}(\pi - 2\alpha_3 - 2\beta_1) + m_{12}(\pi - 2\alpha_2 - 2\beta_1) \}$
Port current equations for EPM-Case B	
$i_{P1 \max}$	$\frac{V_1}{2\omega L} \{ m_{12}(\pi - \beta_2) + m_{13}(\pi - \beta_3) + (2\alpha_2 + 2\beta_2 + 2\alpha_3 + 2\beta_3 - 2\pi) \}$
$i_{P2 \max}$	$\frac{V_1}{2\omega L} \{ m_{12}(2\alpha_2) + m_{13}(\pi - 2\alpha_3 - \beta_3) + (2\alpha_2 + 2\beta_2 - \pi) \}$
$i_{P3 \max}$	$\frac{V_1}{2\omega L} \{ m_{12}(\pi - 2\alpha_2 - \beta_2) + m_{13}(2\alpha_3) + (2\alpha_3 + 2\beta_3 - \pi) \}$

**Table 4** Port current expressions for EPM-Case C

Time interval	Port current expressions
$(0 \leq \alpha_2 \leq (\alpha_2 + \beta_2) \leq \beta_1 \leq \pi)$	$i_{P1max} = \frac{V_1}{2\omega L} [m_{13} (2\alpha_3 + 2\beta_1 - \pi) + m_{12} (\pi - \beta_2)]$ $i_{P2max} = \frac{V_1}{2\omega L} [m_{12} (2\alpha_2) + m_{13} (\pi - 2\alpha_3 - 2\beta_1) + (\beta_1 - \pi)]$
$(0 \leq \alpha_2 \leq \beta_1 \leq (\alpha_2 + \beta_2) \leq \pi)$	$i_{P1max} = \frac{V_1}{2\omega L} [2 (\alpha_2 - \beta_1) + m_{13} (2\alpha_3 + 2\beta_1 - \pi) + m_{12} (\pi + \beta_2)]$ $i_{P2max} = \frac{V_1}{2\omega L} [(2\alpha_2 - \beta_1 - \pi) + 2m_{12} (\alpha_2 + \beta_2) + m_{13} (\pi - 2\alpha_3 - 2\beta_1)]$
$(0 \leq \beta_1 \leq \alpha_2 \leq (\alpha_2 + \beta_2) \leq \pi)$	$i_{P1max} = \frac{V_1}{2\omega L} [2 (\alpha_2 + \beta_2 - \beta_1) + m_{13} (2\alpha_3 + 2\beta_1 - \pi) + m_{12} (\beta_2 + \pi)]$ $i_{P2max} = \frac{V_1}{2\omega L} [(2\alpha_2 + 2\beta_2 - \beta_1 - \pi) + 2m_{12} (\alpha_2 + \beta_2) + m_{13} (\pi - 2\alpha_3 - 2\beta_1)]$
$i_{P3max} = \frac{V_1}{2\omega L} \{ (\pi - \beta_1) + 2m_{13} (2\alpha_3 + 2\beta_1 - \pi) + m_{12} (\pi - 2\alpha_2 - \beta_2) \}$	

**Table 5** Port current expressions for EPM-Case D

Time interval	Port current expressions
$(0 \leq \alpha_3 \leq (\alpha_3 + \beta_3) \leq \beta_1 \leq \pi)$	$i_{P1max} = \frac{V_1}{2\omega L} [m_{12} (2\alpha_2 + 2\beta_1 - \pi) + m_{13} (\pi - \beta_3)]$ $i_{P3max} = \frac{V_1}{2\omega L} [m_{13} (2\alpha_3) + m_{12} (\pi - 2\alpha_2 - 2\beta_1) + (\beta_1 - \pi)]$
$(0 \leq \alpha_3 \leq \beta_1 \leq (\alpha_3 + \beta_3) \leq \pi)$	$i_{P1max} = \frac{V_1}{2\omega L} [2 (\alpha_3 - \beta_1) + m_{12} (2\alpha_2 + 2\beta_1 - \pi) + m_{13} (\pi + \beta_3)]$ $i_{P3max} = \frac{V_1}{2\omega L} [(2\alpha_3 - \beta_1 - \pi) - m_{12} (2\alpha_2 + 2\beta_1 - \pi) + 2m_{13} (\alpha_3 + \beta_3)]$
$(0 \leq \beta_1 \leq \alpha_3 \leq (\alpha_3 + \beta_3) \leq \pi)$	$i_{P1max} = \frac{V_1}{2\omega L} [2 (\alpha_3 + \beta_3 - \beta_1) + m_{12} (2\alpha_2 + 2\beta_1 - \pi) + m_{13} (\beta_3 + \pi)]$ $i_{P3max} = \frac{V_1}{2\omega L} [(2\alpha_3 + 2\beta_3 - \beta_1 - \pi) - m_{12} (2\alpha_2 + 2\beta_1 - \pi) + 2m_{13} (\alpha_3 + \beta_3)]$
$i_{P2max} = \frac{V_1}{2\omega L} \{ (\pi - \beta_1) + 2m_{12} (2\alpha_2 + 2\beta_1 - \pi) + m_{13} (\pi - 2\alpha_3 - \beta_3) \}$	

to be selected, where a least value of current should flow through the converter. Figure 7a depicts the current characteristics with reference to voltage transformation ratio at different values of  $\beta_1$ . Here,  $\beta_1$  equal to zero represents TPM current curve, where TPM current equations is obtained from Table 3, by putting  $\beta_1$  equal to zero. The peak current through the converter is reduced, by incrementing  $\beta_1$  values. From this graph, for a required voltage transformation ratio  $m_{12}$ , the current flowing through port 1 can be selected by appropriately choosing a specific value of  $\beta_1$ . This  $\beta_1$  value is then correlated with the power transfer characteristics in Fig. 5 to substantiate the amount of power demand. However, this computational method does not yield optimum value of phase-shift angles. Therefore, a nonlinear optimization method is adapted to determine the optimized values of phase-shift angles to minimize the current flowing through the ports. Here the target function is to reduce the current flowing through port 1, for this  $i_{P1max}$  expression is assigned as the target function. The expression of  $i_{P1max}$  is chosen as per the state of voltage transformation ratio. Consider EPM-Case C:  $(m_{13} \leq 1) \wedge (m_{12} > 1)$  where the required power level is fixed at  $P_1=750W$ ,  $P_2=500W$  and  $P_3=250W$ . The target function is assigned as per equations in Table 4; from this, the current equation corresponding to medium-power range is selected. The equality constraints are represented by (8) and (9). Inequality constraints are stated in Eq. (10) as per the bounds detailed as  $0 \leq \beta_1 \leq \pi$ ,  $0 \leq \alpha_2 \leq$

$\pi$ ,  $0 \leq \beta_2 \leq \pi$ ,  $0 \leq \alpha_3 \leq \pi$ ,  $0 \leq (\beta_1 + \alpha_2 + \beta_2) \leq \pi$  and  $0 \leq (\beta_1 + \alpha_3) \leq \pi$ . The lower and higher bounds are defined as  $[0, \pi]$ .

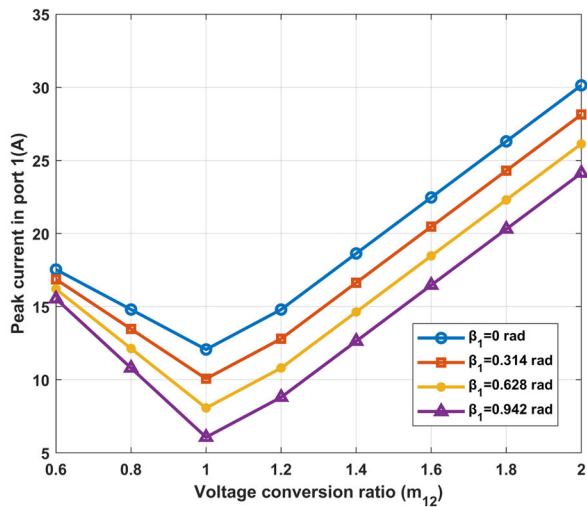
$$C_{eq(1)} = \left\{ \frac{P_{13}\omega\pi L}{V_1^2 m_{13}} - \left[ \begin{array}{c} \alpha_3 (\pi - \alpha_3) \\ +0.5\beta_1 (\pi - \beta_1 - 2\alpha_3) \end{array} \right] \right\} \quad (8)$$

$$C_{eq(2)} = \left\{ \frac{P_{12}\omega\pi L}{V_1^2 m_{12}} - \left[ \begin{array}{c} 2\alpha_2 (\pi - \beta_2) \\ +\beta_2 (\pi - \beta_2 + \beta_1) \\ -\beta_1 - \alpha_2^2 \end{array} \right] \right\} \quad (9)$$

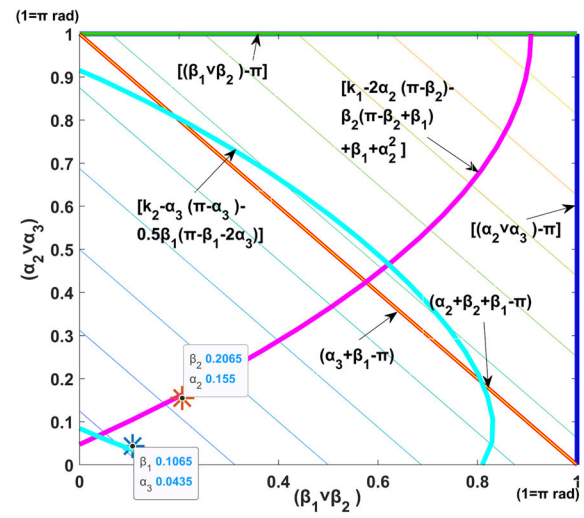
$$\left. \begin{array}{l} C_{(1)} = (\beta_1 - \pi), C_{(2)} = (\alpha_2 - \pi), \\ C_{(3)} = (\beta_2 - \pi), C_{(4)} = (\alpha_3 - \pi), \\ C_{(5)} = (\beta_1 + \alpha_2 + \beta_2 - \pi), \\ C_{(6)} = (\beta_1 + \alpha_3 - \pi). \end{array} \right\} \quad (10)$$

In Fig. 7b, a contour of target function for EPM is plotted and feasible region with potential solutions is obtained by applying equality and inequality constraints. The inequality constraints is expressed as  $[(\beta_1 \vee \beta_2) - \pi], [(\alpha_2 \vee \alpha_3) - \pi], [\alpha_3 + \beta_1 - \pi]$  and  $[\alpha_2 + \beta_2 + \beta_1 - \pi]$ , the equality constraint accounted are  $[k_1 - 2\alpha_2 (\pi - \beta_2) - \beta_2 (\pi - \beta_2 + \beta_1) + \beta_1 + \alpha_2^2]$  and  $[k_2 - \alpha_3 (\pi - \alpha_3) - 0.5\beta_1 (\pi - \beta_1 - 2\alpha_3)]$  where  $k_1 = (\frac{P_{12}\omega\pi L}{V_1^2 m_{12}})$  and  $k_2 = (\frac{P_{13}\omega\pi L}{V_1^2 m_{13}})$ . The optimum solution attained is  $\alpha_2 = 0.155\pi$  rad,  $\beta_2 = 0.2065\pi$  rad,  $\beta_1 = 0.1065\pi$  rad and  $\alpha_3 = 0.0435\pi$  rad with target function settling at  $i_{P1max}=10A$ .The optimal result obtained is

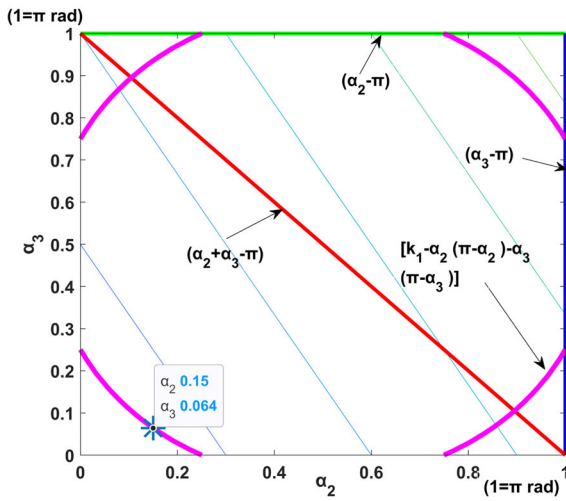




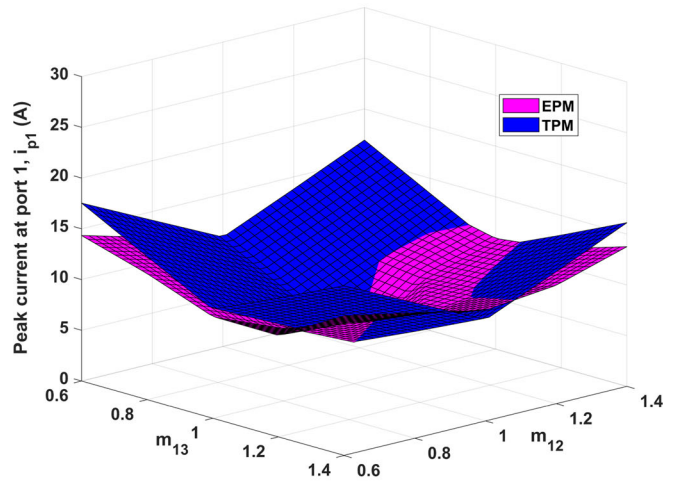
(a)



(b)



(c)



(d)

**Fig. 7** (a) Flexibility in port 1 current characteristics with reference to  $m_{12}$  at different values of  $\beta_1$ . (b) Contour plot of target function with constraints under EPM scheme. (c) Contour plot of target function with

constraints under TPM scheme. (d) 3-D plot of converter peak current stress with reference to  $m_{12}$  and  $m_{13}$  in port 1 under EPM and TPM schemes

marked in Fig. 7b, the points attained is aligned with the equality constraints and is within the boundary of inequality constraints. Similar case is evaluated under TPM technique. The optimal solution achieved is indicated in the contour plot of Fig. 7c. The operating points at which the target function becomes minimum are  $\alpha_2 = 0.15\pi$  rad and  $\alpha_3 = 0.064\pi$  rad with the least base at  $i_{p1max} = 13.67$ A. Three-dimensional plot of target function with reference to  $m_{12}$  and  $m_{13}$  varying from 0.6 to 1.4 under both EPM and TPM scheme is illustrated in Fig. 7d, where the target function is minimized to a least value in EPM scheme compared with TPM, except at points near to unity.

Figure 8a–d illustrates comparison of peak current across port 1 under both EPM and TPM with reference to  $m_{13}$  keeping  $m_{12}$  constant. In case with  $m_{12} = 0.6$  shown in Fig. 8a, EPM limits the current at all values of  $m_{13}$  from 0.6 to 1.4. The case where  $m_{12} = 0.8$  is depicted in Fig. 8b, which is around the nominal value, the current stress reduction range between EPM and TPM is reduced as related to the earlier case. The peak current value is almost coinciding at  $(m_{12}, m_{13}) = (0.8, 1)$ . Figure 8c reflects the case where  $m_{12} = 1.2$ , here, EPM outperforms in all combinations of  $m_{13}$  except at combination  $(m_{12}, m_{13}) = (1.2, 1)$ , where 8.22% of deterioration is observed for EPM. In Fig. 8d, the lower-

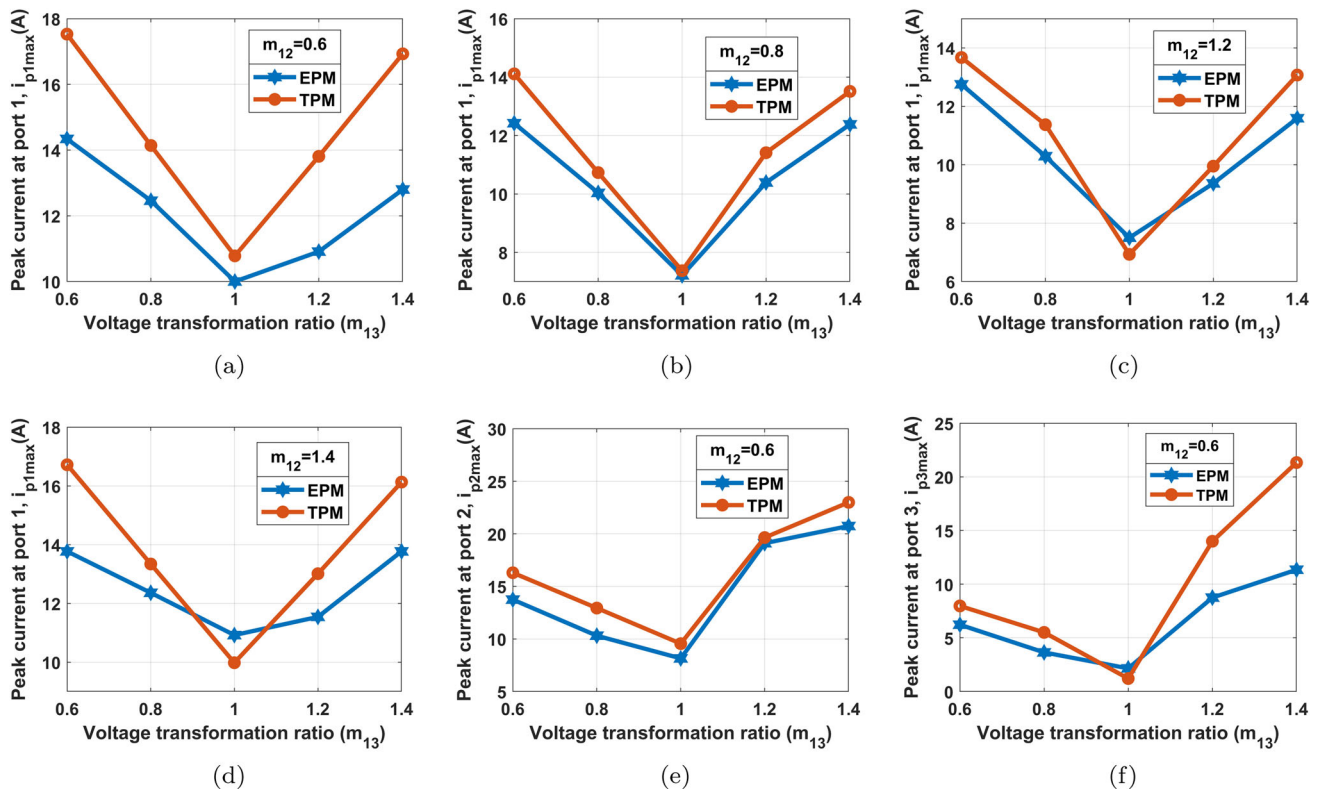


**Fig. 8** Comparison of peak current between EPM and TPM techniques. (a) In port 1 with respect to  $m_{13}$  at  $m_{12} = 0.6$ . (b) In port 1 with respect to  $m_{13}$  at  $m_{12} = 0.8$ . (c) In port 1 with respect to  $m_{13}$  at  $m_{12} = 1.2$ . (d)

In port 1 with respect to  $m_{13}$  at  $m_{12} = 1.4$ . (e) In port 2 with reference to  $m_{13}$  keeping  $m_{12} = 0.6$ . (f) In port 3 with reference to  $m_{13}$  keeping  $m_{12} = 0.6$

ing limits of current stress is more by employing EPM when  $m_{12} = 1.4$ . The following graphs indicate that when the voltage transformation ratio is away from the nominal value, unity, the reduction range of current stress is more in EPM scheme. Figure 8e and f represents the reduction in peak current by utilizing EPM at port 2 and port 3, respectively, with reference to voltage transformation ratio.

### 3 Hardware implementation and experimental results

A 1.5kW hardware prototype of 3PIHC is developed, and the experimental results are evaluated, which authenticates with the theoretical analysis. The primary side of 3PIHC is a multilevel half-bridge circuit, where the switch voltage is reduced to half of the supply voltage.

The semiconductor switches adopted for primary, secondary and tertiary side are SiHG32N50D, IRFB4227PbF and IRFB4110PbF, respectively. Converter switching frequency is selected as 50kHz considering the size and losses in the high-frequency transformer. Permanent magnet ferrite core 62/49 is opted for fabricating high-frequency trans-

**Table 6** Experimental standards of 3PIHC

Definitions	Standards
Port 1 DC Voltage ( $V_{in}$ )	300~400V
Port 2 DC Voltage ( $V_{o1}$ )	40~170V
Port 3 DC Voltage ( $V_{o2}$ )	20~70V
Switching frequency, $f_s$	50kHz
Power at Port 1	200~1500W
Power at Port 2	150~1000W
Power at Port 3	50~500W
$N_1 : N_2 : N_3$	25:15:6
$L_{12}, L_{13}, L_{32}$	20uH,20uH,20uH

former. The transformer turns ratio and size of litz wires are decided by considering voltage transformation ratio and current through the winding, respectively. The switching signals for 3PIHC are generated using DSP board F28335. Experimental set-up of 3PIHC is shown in Fig. 9, and the hardware specification are detailed in Table 6.

Here the target is to reduce current through port 1 by considering the constraints of power demand and voltage transformation ratio. The 3PIHC circuit is tested under both

**Fig. 9** Experimental set-up of three-port isolated hybrid converter

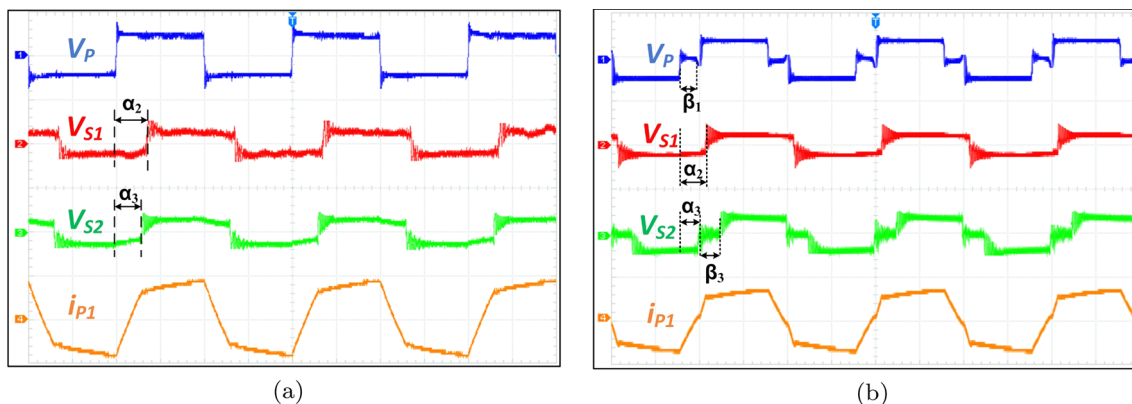
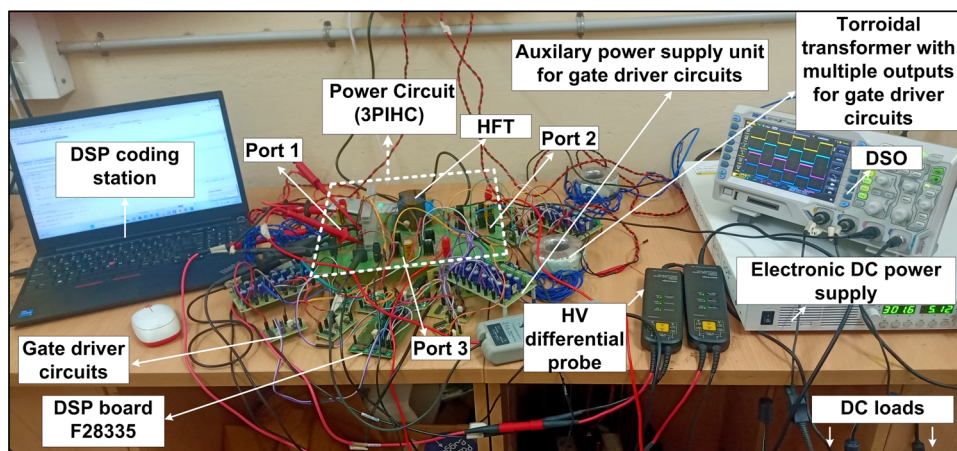


**Fig. 10** Experimental waveforms of 3PIHC (a)  $V_p$  (400V/div),  $V_{S1}$  (325V/div),  $V_{S2}$  (200V/div),  $i_{P1}$  (13A/div) under TPM. (b)  $V_p$  (450V/div),  $V_{S1}$  (325V/div),  $V_{S2}$  (150V/div),  $i_{P1}$  (13A/div) under EPM (time division:  $5\mu s/div$ )

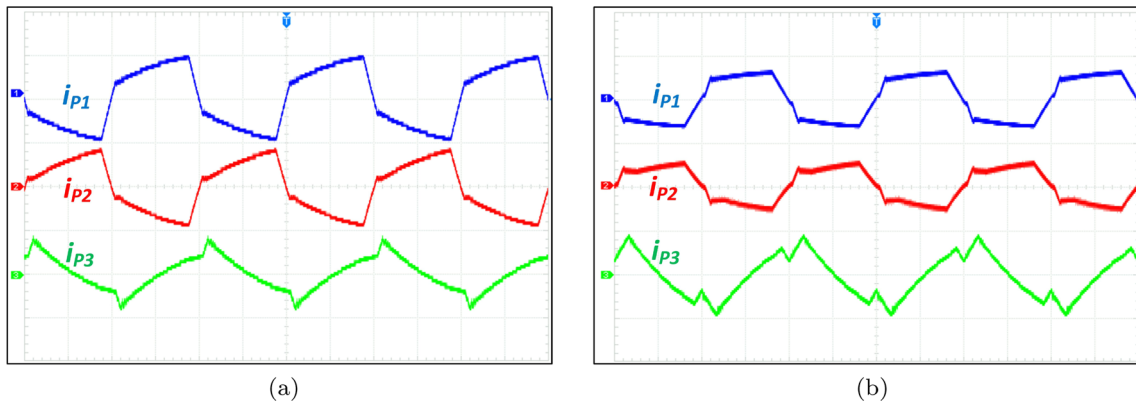
**Table 7** Power loss expressions to calculate losses in 3PIHC

Description	Expression
Switch turn-off losses	$(V_{DD1}I_{D1(on)}t_{off1}) \frac{f_{sw}}{2} + (V_{DD2}I_{D2(on)}t_{off2}) \frac{f_{sw}}{2} + (V_{DD3}I_{D3(on)}t_{off3}) \frac{f_{sw}}{2}$
Switch conduction losses	$I_{Drms1}^2 R_{DS1(on)} + I_{Drms2}^2 R_{DS2(on)} + I_{Drms3}^2 R_{DS3(on)}$
Transformer core losses	$k_w f_{sw}^\alpha B_m^\beta$
Transformer copper losses	$I_{rms1}^2 R_{wdg1} + I_{rms2}^2 R_{wdg2} + I_{rms3}^2 R_{wdg3}$
Gate driver losses	$C_{iss1} V_g^2 f_{sw} + C_{iss2} V_g^2 f_{sw} + C_{iss3} V_g^2 f_{sw}$
Diode recovery losses	$Q_{RR1} V_{d1} \frac{f_{sw}}{2} + Q_{RR2} V_{d2} \frac{f_{sw}}{2} + Q_{RR3} V_{d3} \frac{f_{sw}}{2}$

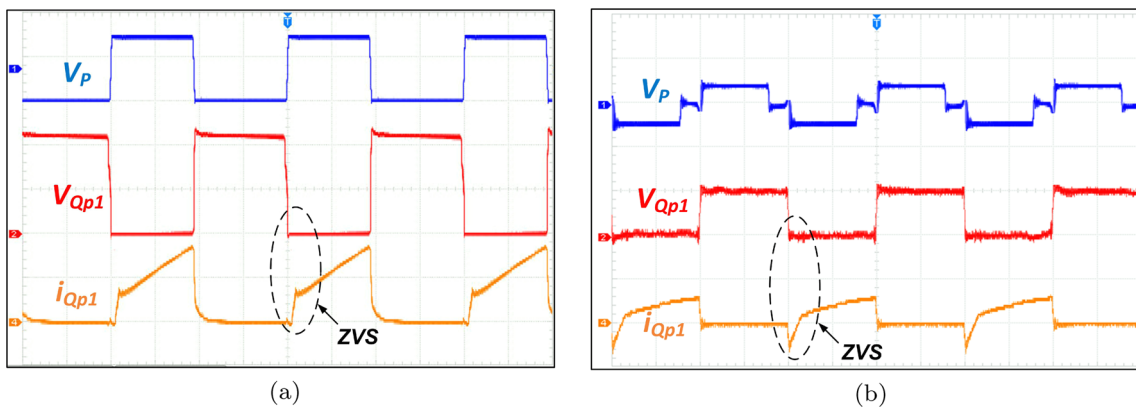
\*All variables are defined in Appendix

EPM and TPM schemes, here the conditions accounted for illustrating the experimental waveforms are with a power level of  $P_1=750W$ ,  $P_2=500W$  and  $P_3=250W$  and voltage transformation ratio as  $m_{12} = 0.8$  and  $m_{13} = 1.2$ . Optimum value of phase-shift angles is determined to attain minimum value of current stress in the converter. Transformer  $1^0$ ,  $2^0$  and  $3^0$  voltages obtained under TPM are presented in Fig. 10a; here, the transformer  $1^0$  voltage is equal to half of the supply voltage. The transformer secondary and tertiary voltage is same as per the respective port voltages and is phase-shifted at optimum angles of  $\alpha_2 = 0.453$  rad

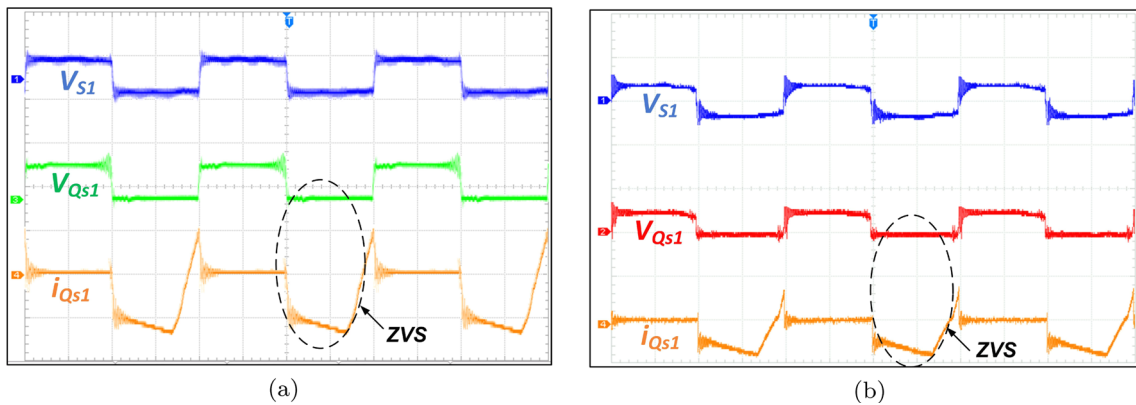
and  $\alpha_3 = 0.366$  rad with respect to primary voltage. The current through port 1 ( $i_{P1}$ ) in TPM is depicted in Fig. 10a along with the transformer voltages and it holds a peak value of 10.4A. The waveforms obtained by applying EPM for the same operating conditions are shown in Fig. 10b, where the phase-shift values applied are  $\alpha_2 = 0.85$  rad,  $\alpha_3 = 0.659$  rad,  $\beta_1 = 0.62$  rad and  $\beta_3 = 0.78$  rad. By employing EPM, the current through port 1 is reduced to 9.41A, where a reduction in current stress of 9.5% is attained and also the three-level voltage waveforms across primary and tertiary winding will reduce core losses in the transformer when compared to TPM.



**Fig. 11** Experimental waveforms of 3PIHC (a)  $i_{P1}$ (11A/div),  $i_{P2}$  (24A/div),  $i_{P3}$ (75A/div) under TPM. (b)  $i_{P1}$  (15A/div),  $i_{P2}$  (32A/div),  $i_{P3}$ (50A/div) under EPM (time division:5 $\mu$ s/div)



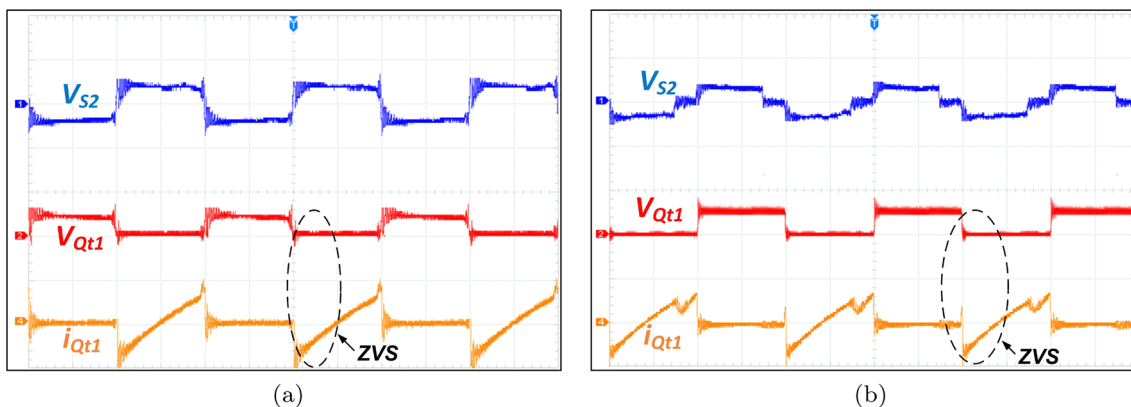
**Fig. 12** Experimental waveforms of 3PIHC (a)  $V_P$ (275V/div),  $V_{Qp1}$  (90V/div),  $i_{Qp1}$ (4A/div) under TPM. (b)  $V_P$  (450V/div),  $V_{Qp1}$  (200V/div),  $i_{Qp1}$ (10A/div) under EPM (time division:5 $\mu$ s/div)



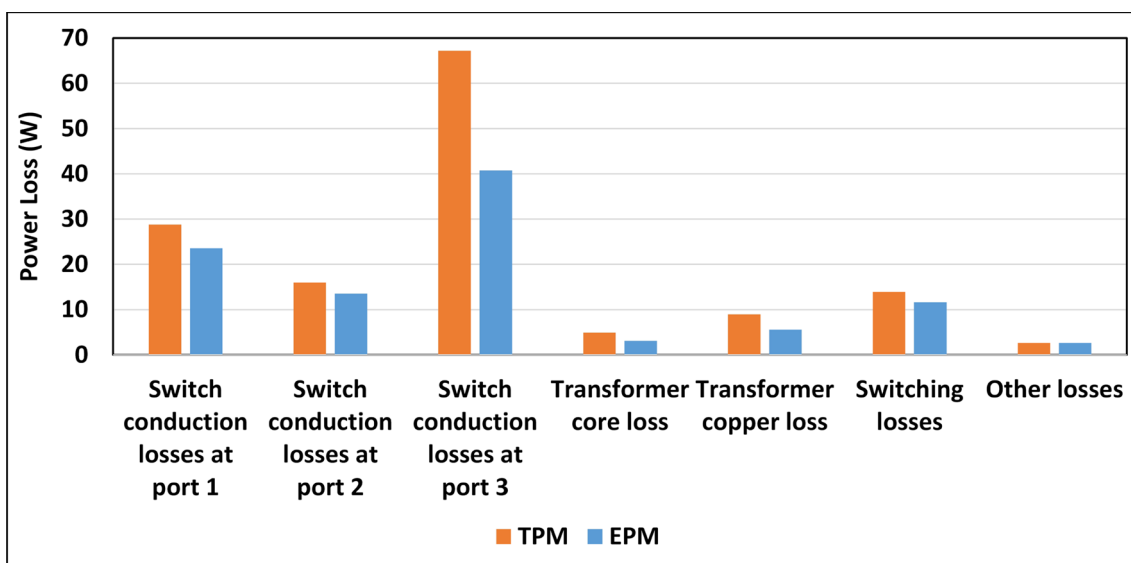
**Fig. 13** Experimental waveforms of 3PIHC (a)  $V_{S1}$ (200V/div),  $V_{Qs1}$  (110V/div),  $i_{Qs1}$ (15A/div) under TPM. (b)  $V_{S1}$  (320V/div),  $V_{Qs1}$  (200V/div),  $i_{Qs1}$ (18A/div) under EPM (time division:5 $\mu$ s/div)

Figure 11a depicts primary, secondary and tertiary currents through the transformer under TPM, which hold values of 10.39A, 21.38A and 62A, respectively. Similarly, the transformer current waveforms under EPM is displayed in

Fig. 11b, where the values for  $i_{P1}$ ,  $i_{P2}$  and  $i_{P3}$  are 9.41A, 19.5A and 47.5A, respectively. In this, a reduction in current stress of 9.5%, 8.79% and 23.3% is attained at port 1, port 2 and port 3 respectively. Transformer 1<sup>0</sup> voltage together with



**Fig. 14** Experimental waveforms of 3PIHC (a)  $V_{S2}$ (160V/div),  $V_{Qt1}$  (145V/div),  $i_{Qt1}$ (60A/div) under TPM. (b)  $V_{S2}$  (160V/div),  $V_{Qt1}$  (115V/div),  $i_{Qt1}$ (75A/div) under EPM (time division:5 $\mu$ s/div)



**Fig. 15** Power loss distribution in 3PIHC with TPM and EPM schemes

switch voltage and current of port 1 under TPM is illustrated in Fig. 12a. Here switch  $Q_{p1}$  is turned ON at zero voltage switching (ZVS) and holds a value of 6.93A. The same is correlated with EPM and is shown in Fig. 12b, where current through the switch is decreased by 9.5%, and ZVS is achieved explicitly for  $Q_{p1}$ .

The voltage and current waveforms of switch in port 2 together with voltage across  $2^0$  side of the transformer at TPM and EPM are demonstrated in Fig. 13a and b, respectively. Here the switch current  $i_{Qs1}$  is reduced to 8.13% in EPM scheme. Similarly, voltage and current waveforms of switch in port 3 together with transformer  $3^0$  voltage at TPM and EPM are illustrated in Fig. 14a and b, respectively. Here a reduction in current stress of 22.14% is observed for  $i_{Qt1}$  under EPM.

The expressions employed for power loss calculations in the converter are given in Table 7. The power loss distribution for 3PIHC are evaluated from the experimental results and is presented in Fig. 15. The switch conduction losses is reduced in all ports by applying EPM, and the percentage reductions of losses are 17.99%, 15.55% and 39.36%, respectively, at port 1, port 2 and port 3. Due to high-current and low-voltage configuration, port 3 exhibits more reduction in conduction losses. The three-level voltage waveforms at the transformer windings in EPM reduce the core losses to 37.85%. The current stress reduction aids in minimizing the transformer copper loss to 37.90%. All the semiconductor switches are turned on at ZVS; therefore, only turn-off losses are accounted. The turn-off switching losses is minimized to 16.28% in EPM. Other losses which includes diode recovery

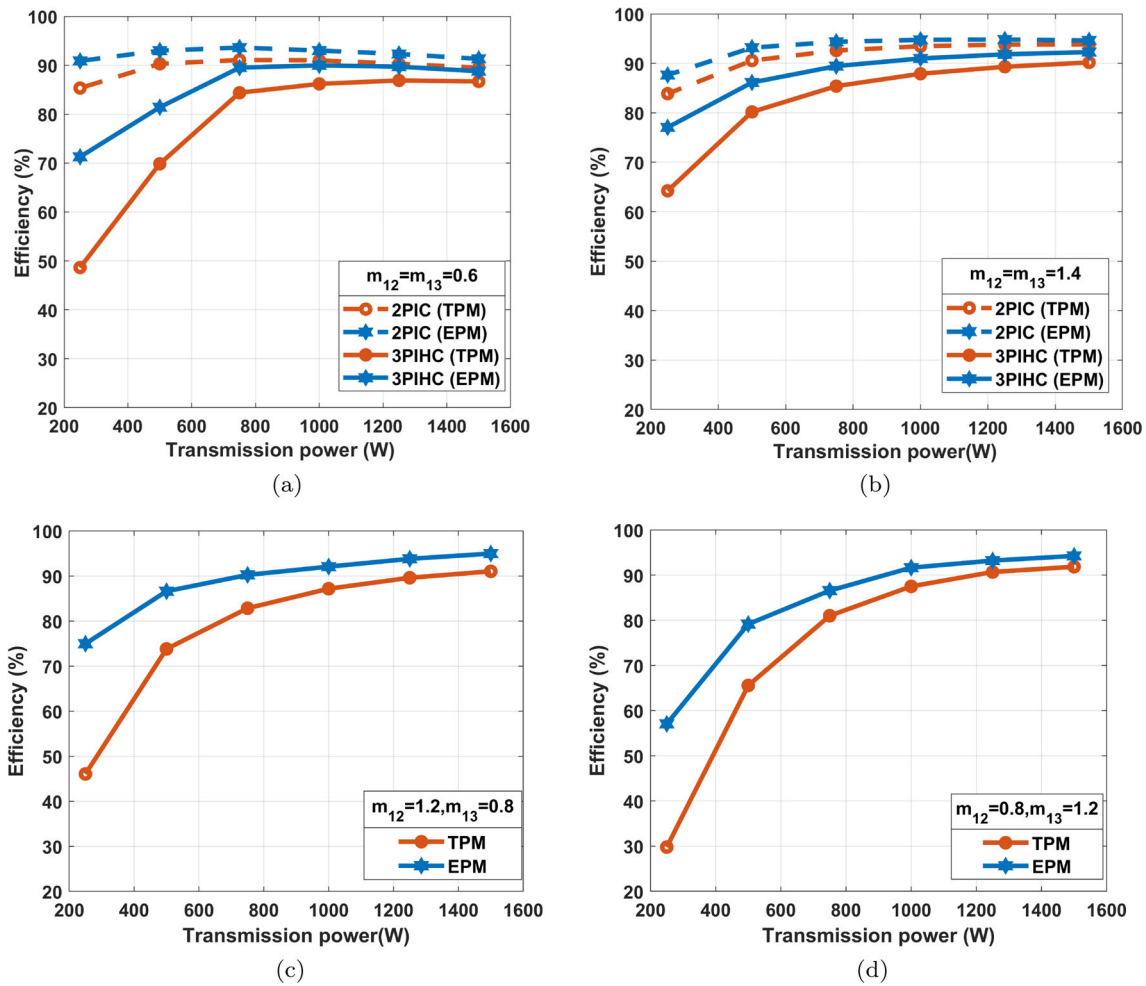


**Fig. 16** Efficiency characteristics of 3PIHC with TPM and EPM schemes. (a) EPM-Case A:  $(m_{12} \wedge m_{13}) \leq 1$ . (b) EPM-Case B:  $(m_{12} \wedge m_{13}) > 1$ . (c) EPM-Case C:  $(m_{13} \leq 1) \wedge (m_{12} > 1)$ . (d) EPM-Case D:  $(m_{12} \leq 1) \wedge (m_{13} > 1)$

losses, gate driver losses and ESR of filters/parasitics remain same for both modulation.

The efficiency characteristics of 3PIHC in all possible cases with EPM and TPM are plotted in Fig. 16. The overall efficiency is decreased when operating the converter away from the nominal value of voltage conversion ratios. The peak efficiency at  $m_{12} = m_{13} = 0.6$  in TPM and EPM is 86.90% and 89.70%, respectively, and the peak efficiency at  $m_{12} = m_{13} = 1.4$  in TPM and EPM is 90.17% and 92.28%, respectively. For EPM-Case C when  $m_{12} = 1.2, m_{13} = 0.8$ , the efficiency gained in TPM and EPM is 91.03% and 94.96%, respectively. For EPM-Case D where  $m_{12} = 0.8, m_{13} = 1.2$ , the efficiency attained is 91.85% and 94.24% for TPM and EPM, respectively. From the above efficiency characteristics, it is evident that by employing EPM scheme the converter performance is enhanced, particularly at low-power regions and at wide change in voltage transformation ratios. The efficiency characteristics obtained for the cases  $m \leq 1$  and

$m > 1$  in 2PIC are plotted in Fig. 16a and b, respectively, which implies an increased efficiency for 2PIC compared to 3PIC, due to less number of semiconductor switches. The limitations of the proposed work are as mentioned below,

1. The predominant losses in the converter are due to conduction losses. Solution to minimize this is by employing switches with high-temperature handling capability and low  $R_{DS(ON)}$ , i.e. silicon carbide (SiC) switches, gallium nitride (GaN) switches and surface-mounted MOSFETs. Due to the cost constraints, the authors are not able to utilize wide-band-gap devices for further reducing the conduction losses in the proposed topology.
2. Here the optimized phase-shift variables at minimum current stress is obtained by nonlinear optimization techniques, which is complex to implement in digital controllers. Therefore, the optimized phase-shift param-

eters for TPM and EPM are priorly determined by mathematical software (MATLAB). Based on the computed optimized variables, a database look-up table is formed and is loaded in the DSP control board. Accuracy and improved results can be obtained with increased database with continuous updation, as the inherent characteristics of the converter vary.

## 4 Conclusions

This paper addresses the issue of high current stress in 3PIHC when operating at wide variation in voltage transformation ratio. The hardware prototype of 3PIHC is tested under both TPM and EPM schemes and presented the results. Theoretical analysis and experimental results validates that the power loss due to mismatch in voltage transformation ratios is minimized by employing EPM strategy, especially at light load conditions. Examined the power loss distribution in 3PIHC under both modulation techniques, a remarkable reduction in switch conduction loss, transformer core loss and copper loss are noticed with EPM. It is a cost-effective form of method to increase the efficiency of 3PIHC, without any additional sub-circuits. Efficiency characteristics reveals that by employing EPM in 3PIHC improves the utilization of power generation and performance of power converters. The future scope of this proposed work are listed below,

1. Developing a power loss optimized algorithm for computing phase-shift variables will significantly increase the converter's efficiency to a great extent.
2. According to the application requirement, circulating power flow minimization can also be included in the converter. In addition to this, soft switching boundary condition can be added in the constraints to ensure soft switching condition for the entire power transfer range.

**Author Contributions** SS was responsible for theoretical analysis, hardware design and testing, and manuscript writing. SS was responsible for hardware testing, evaluation of hardware results and manuscript correction.

**Funding** We wish to confirm that no funding was received for this work.

**Data Availability** This declaration is not applicable.

## Declarations

**Conflict of interest** We wish to confirm that there are no competing interests of a financial or personal nature.

**Ethical approval** This declaration is not applicable. We wish to confirm that there is no human and/or animal studies involved in this work.

## Appendix

$B_m$	Peak magnetic flux density
$C_{iss1}, C_{iss2}, C_{iss3}$	Switch input capacitance in port 1, port 2 and port 3, respectively.
$f_{sw}$	Switching frequency
$I_{(D1(on))}, I_{(D2(on))}, I_{(D3(on))}$	Drain current in port 1, port 2 and port 3, respectively.
$I_{Drms1}, I_{Drms2}, I_{Drms3}$	RMS value of switch current in port 1, port 2 and port 3, respectively
$k_w, \alpha, \beta$	Steinmetz coefficients
$Q_{RR1}, Q_{RR2}, Q_{RR3}$	Reverse recovery charge of switches in port 1, port 2 and port 3, respectively.
$R_{(DS1(on))}, R_{(DS2(on))}, R_{(DS3(on))}$	Drain source resistance in port 1, port 2 and port 3, respectively
$R_{wdg1}, R_{wdg2}, R_{wdg3}$	Winding resistance at port 1, port 2 and port 3, respectively
$t_{off1}, t_{off2}, t_{off3}$	Overlap time between switch voltage and current in port 1, port 2 and port 3, respectively
$V_{d1}, V_{d2}, V_{d3}$	Diode forward voltage across the switches in port 1, port 2 and port 3, respectively.
$V_g$	Switch driving voltage
$V_{DD1}, V_{DD2}, V_{DD3}$	Drain to source voltage in port 1, port 2 and port 3, respectively

## References

1. Kassakian JG, Miller JM, Traub N (2000) Automotive electronics power up. *IEEE Spectrum* 37(5):34–39
2. Pham VL, Wada K (2020) Applications of triple active bridge converter for future grid and integrated energy systems. *Energies* 3(7):1577
3. Piris-Botalla L, Oggier GG, García GO (2017) Extending the power transfer capability of a three-port DC-DC converter for hybrid energy storage systems. *IET Power Electron* 10(13):1687–1697
4. Krishnaswami H, Mohan N (2009) Three-port series-resonant DC-DC converter to interface renewable energy sources with bidirectional load and energy storage ports. *IEEE Trans Power Electron* 24(10):2289–2297
5. Dev MA, Babu KTH, Beevi PF (2022) Three Mode Three-Port Isolated DC/DC Converter With Dual Fast Charging Port. In: International Conference on Futuristic Technologies in Control Systems and Renewable Energy (ICFCR), Malappuram, India, pp 1–6. <https://doi.org/10.1109/ICFCR54831.2022.9893609>
6. Piris-Botalla L, Oggier CG, Airabella AM, García GO, (2014) Power losses evaluation of a bidirectional three-port DC-DC converter for hybrid electric system. *Int J Electr Power Energy Syst.* <https://doi.org/10.1016/j.ijepes.2013.12.021>
7. Jakka VNSR, Shukla A, Demetriades GD (2017) Dual-Transformer-based asymmetrical triple-port active bridge (DT-ATAB) isolated DC-DC converter. *IEEE Trans Ind Electron* 64(6):4549–4560
8. Sim J (2020) Research on advanced three-port dual-active-bridge (DAB) converters for DC microgrid. Web
9. Van-Long P, Keiji W (2020) Normalization design of inductances in triple active bridge converter for household renewable energy system. *IEEJ J Ind Appl* 9(3):227–234

10. Chen Y-M, Liu Y-C, Wu F-Y (2002) Multi-input DC/DC converter based on the multiwinding transformer for renewable energy applications. *IEEE Trans Ind Appl* 38(4):1096–1104. <https://doi.org/10.1109/TIA.2002.800776>
11. Tao H, Duarte JL, Hendrix MAM (2008) Three-Port Triple-Half-Bridge Bidirectional Converter With Zero-Voltage Switching. *IEEE Transactions on Power Electronics* 23(2):782–792
12. Neng Z, Danny S, Muttaqi Kashem M (2016) A review of topologies of three-port dc to dc converters for the integration of renewable energy and energy storage system. *Renew Sustain Energy Rev* 56:388–401. <https://doi.org/10.1016/j.rser.2015.11.079>
13. Rahrovi B, Mehrjardi RT, Ehsani M (2021) On the analysis and design of high-frequency transformers for dual and triple active bridge converters in more electric aircraft. In: *IEEE Texas Power and Energy Conference (TPEC)*, College Station, TX, USA, pp 1–6. <https://doi.org/10.1109/TPEC51183.2021.9384990>
14. Kheraluwala M, Gascoigne R, Divan D, Baumann E (1992) Performance characterization of a high-power dual active bridge DC-to-DC converter. *IEEE Trans Ind Appl* 10(1109/28):175280
15. Naayagi RT, Forsyth AJ, Shuttleworth R (2012) High-power bidirectional DC-DC converter for aerospace applications. *IEEE Trans Power Electron*. <https://doi.org/10.1109/TPEL.2012.2184771>
16. Zhao C, Round SD, Kolar JW (2008) An isolated three-port bidirectional DC-DC converter with decoupled power flow management. *IEEE Trans Power Electron* 23(5):2443–2453. <https://doi.org/10.1109/TPEL.2008.2002056>
17. Tao H, Kotsopoulos A, Duarte JL, Hendrix MAM (2008) Transformer-coupled multiport ZVS bidirectional DC-DC converter with wide input range. *IEEE Trans Power Electron* 23(2):771–781. <https://doi.org/10.1109/TPEL.2007.915129>
18. Zou S, Lu J, Khaligh A (2020) Modelling and control of a triple-active-bridge converter. *IET Power Electron*. <https://doi.org/10.1049/iet-pel.2019.0920>
19. Sofiya S, Sathyan S (2023) A three-level three port isolated converter with reduced current stress for DC microgrid applications. *Int J Circ Theor Appl*. <https://doi.org/10.1002/cta.3572>
20. Hiltunen J, Väisänen V, Juntunen R, Silventoinen P (2015) Variable-frequency phase shift modulation of a dual active bridge converter. *IEEE Trans Power Electron* 30(12):7138–7148
21. Jain AK, Ayyanar R (2011) Pwm control of dual active bridge: comprehensive analysis and experimental verification. *IEEE Trans Power Electron*. <https://doi.org/10.1109/TPEL.2010.2070519>
22. Zhao B, Song Q, Liu W, Sun Y (2014) Overview of dual-active-bridge isolated bidirectional DC-DC converter for high-frequency-link power-conversion system. *IEEE Trans Power Electron*. <https://doi.org/10.1109/TPEL.2013.2289913>
23. Rodriguez A, Vazquez A, Lamar DG, Hernando MM, Sebastian J (2015) Different purpose design strategies and techniques to improve the performance of a dual active bridge with phase-shift control. *IEEE Trans Power Electron* 30(2):790–804. <https://doi.org/10.1109/TPEL.2014.2309853>
24. Zhao B, Yu Q, Sun W (2012) Extended-phase-shift control of isolated bidirectional DC-DC converter for power distribution in microgrid. *IEEE Trans Power Electron* 27(11):4667–4680
25. Moonem MA, Krishnaswami H (2012) Analysis and control of multi-level dual active bridge DC-DC converter. *IEEE Energy Convers Congress Expos (ECCE) 2012*:1556–1561. <https://doi.org/10.1109/ECCE.2012.6342628>
26. Sofiya S and Sathyan S (2022) Three-Port Isolated Hybrid Converter for Power Supply Systems in EV. In: *2022 IEEE international conference on power electronics, smart grid, and renewable energy (PESGRE)*, pp 1–6. <https://doi.org/10.1109/PESGRE52268.2022.9715948>

**Publisher's Note** Springer Nature remains neutral with regard to jurisdictional claims in published maps and institutional affiliations.

Springer Nature or its licensor (e.g. a society or other partner) holds exclusive rights to this article under a publishing agreement with the author(s) or other rightsholder(s); author self-archiving of the accepted manuscript version of this article is solely governed by the terms of such publishing agreement and applicable law.